Available online at www.sciencedirect.com
ScienceDirect
Trans. Nonferrous Met. Soc. China 35(2025) 1057−1074
Transactions of Nonferrous Metals Society of China
www.tnmsc.cn

Impact of atomization methods on aluminum alloy powder characteristics and 3D printing performance in laser directed energy deposition process

Gang RUAN[1], Yu-dong LIANG[2], Gan LI[1,3], Ying JIN[4], Xing-gang LI[1,2]

1. Department of Mechanical and Energy Engineering,
Southern University of Science and Technology (SUSTech), Shenzhen 518055, China;
2. Department of Materials Science and Engineering,
Southern University of Science and Technology (SUSTech), Shenzhen 518055, China;
3. Department of Mechanical Engineering, City University of Hong Kong, Hong Kong 999077, China;
4. Zhejiang Yatong Advanced Materials Co., Ltd., Hangzhou 310030, China

Received 30 August 2023; accepted 13 May 2024

Abstract: A comparative study on the performance of gas atomized (GA) and rotating-disk atomized (RDA) aluminum alloy powders produced on industrial scale for laser directed energy deposition (L-DED) process was carried out. The powder characteristics, the printing process window, and the quality, microstructure, and mechanical properties of printed parts were taken into account for comparison and discussion. The results demonstrate that the RDA powder is superior to the GA powder in terms of sphericity, surface quality, internal defects, flowability, and apparent density, together with a larger printing process window during the L-DED parts fabrication. Besides, the resultant parts from the RDA powder have higher dimensional accuracy, lower internal defects, more uniform and finer microstructure, and more favorable mechanical properties than those from the GA powder.

Key words: metal additive manufacturing; rotating disk atomization; gas atomization; AlSi10Mg powder; powder feedstocks

1 Introduction

Lightweight design and manufacturing using aluminum alloys offer a promising solution for energy conservation in various industries such as aerospace, transportation, electronics, medical, and chemical, thanks to their low density, high corrosion resistance, and excellent physical and mechanical properties [1−3]. However, conventional manufacturing processes limit the full utilization of aluminum alloys in complex structures. The emergence of metal additive manufacturing (MAM), or 3D printing, has revolutionized the fabrication of complex structures, providing design flexibility and unlocking the maximum potential of alloys [4−6]. Despite notable advancements, previous studies [2,7] have primarily focused on laboratory-scale 3D-printed aluminum alloy components due to the properties and costs associated with the powder feedstocks used in the MAM process. Therefore, it is crucial to identify a suitable process that can produce cost-effective, high-quality aluminum alloy powders to address these challenges.

Additive manufacturing is widely recognized for producing high-quality parts using powders with desirable properties [2,8−11]. Among various methods for preparing powder feedstocks, the gas atomization (GA) process, thanks to its high production efficiency and excellent process

Corresponding author: Xing-gang LI, Tel: +86-755-88018131, E-mail: xing-gangli@163.com, lixg@sustech.edu.cn
DOI: https://doi.org/10.1016/S1003-6326(24)66734-8

controllability [12,13], is favored. As shown in Fig. 1(a), the GA process involves melting ingots in a crucible to enable continuous atomization, producing cost-effective powder [14]. However, satellite and hollow particles are introduced during the process due to turbulent gas flow and interactions among gas, droplets, and particles [12,13]. Satellite particles form when small particles or droplets adhere to larger particles or droplets during spray, negatively affecting powder properties and subsequent processes. Hollow particles result from the gas-entrapped droplets, which may decrease the tensile strength and elongation [14,15] and worse still, affect the notch durability and fatigue performance of the 3D-printed parts [16]. Despite the cost-effectiveness of the GA process in powder preparation, it remains challenging to prevent the formation of excessive satellite particles and hollow particles.

In contrast, centrifugal atomization (CA) is an alternative method for producing powder with high sphericity, smooth surface, and good flowability by leveraging centrifugal force to break apart molten metal, thus reducing the collision frequency between metallic droplets and/or particles [17]. As shown in Fig. 1(b), plasma rotating electrode process (PREP) enables the industrial production of high-quality refractory alloy powders based on nickel [10,18], iron [19], cobalt [19], and titanium [19,20], but it is not suitable for atomizing raw materials with low melting points, low densities, high coefficients of thermal expansion, and high thermal conductivity. It is highly challenging to enhance the fine powder yield of lightweight metals to satisfy MAM requirements through increasing electrode rotating speed [21]. Moreover, the high-energy plasma used in PREP can result in significant loss of alloying elements due to the overheating and evaporation of volatile elements [22]. Although the PREP produces powders with excellent performance, the associated preparation cost is typically several times higher than that of the GA process [16].

Another alternative approach is the rotating disk atomization (RDA) process, which uses centrifugal force to break up molten metal as it falls onto a high-speed rotating disk [23], as depicted in Fig. 1(c). By carefully adjusting parameters such as melt temperature, melt feeding rate, and rotating disk speed during atomization [23−25], high-quality powder characterized by excellent sphericity, uniform particle size, smooth surface, good flowability, and reduced hollow particle content can be prepared. Unlike PREP, the RDA process allows the use of a crucible to melt the ingots, enabling cost-effective and continuous preparation. The rotating disk can achieve exceptionally high speeds of nearly 120000 r/min [26], which can increase the fine powder yield of low-density and high-thermal-conductivity materials such as Al alloys. Additionally, the RDA process uses resistance heating or electromagnetic induction to melt raw materials, allowing for precise temperature control and minimizing the loss of volatile elements. The RDA process has been commercially employed for continuous production of micro-fine spherical powders of low-melting-point metals such as zinc, tin, and magnesium alloys. However, its application in preparing high-quality aluminum alloy powders for MAM processes has received limited attention to date.

In the present work, AlSi10Mg powders were successfully prepared through respective RDA and GA processes. A comparative study on powder

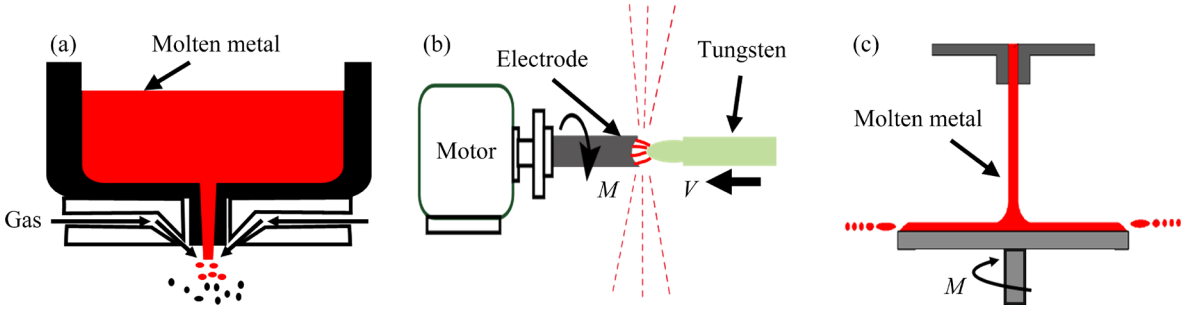

Fig. 1 Metal powder preparation methods for additive manufacturing: (a) Gas atomization (GA); (b) Plasma rotating electrode process (PREP); (c) Rotating disk atomization (RDA) (*M*−Moment of self-consuming electrode or motor shaft rotation; *V*−Velocity of plasma gun movement)

characteristics was conducted concerning the composition, particle size distribution (PSD), morphology, internal defects, flowability, and apparent density of the two powders. The 3D printing performance of the two powders was also investigated by comparing the printing process window and mechanical properties of the 3D-printed parts in the laser directed energy deposition (L-DED) process.

2 Experimental

2.1 Atomization process for powder preparation

In this study, two types of AlSi10Mg alloy powders were produced through GA process and RDA process, respectively, using the same batch of master alloy ingots. For both processes, the melting furnaces and atomization chambers were initially evacuated, and then filled with 99.99% pure nitrogen (N_2) gas to 1.013×10^5 Pa before the atomization. The raw powders were only sieved to a particle size range from 45 to 105 μm without any additional treatment.

The vacuum induction melting gas atomization (VIGA) process was employed, together with a close-coupled configuration between gas nozzle and melt delivery nozzle. The raw ingots of total 150 kg per run were first inductively heated and melted in a graphite crucible, and then the molten metal was poured into a graphite tundish, which was resistively heated and maintained at a constant temperature of 900 °C. Atomization was performed using 99.99% pure N_2 at an atomization pressure of 3.5 MPa with a gas flow rate of approximately 20 L/min. The gas atomization parameters were optimized to achieve a high powder yield in a particle size range of 45−105 μm. A maximum powder yield of about 35% could be obtained.

In the RDA process, raw ingots of total 500 kg per run were inductively heated and melted in a graphite crucible, and then the molten metal was poured into a graphite tundish, which was resistively heated and maintained at a constant temperature of 800 °C. A flat disk with a diameter of 30 mm was used to atomize melts under a rotary speed of 30000 r/min. The disk was made of stainless steel, with its upper surface coated with wear-resistant refractory. Under these conditions, a maximum powder yield of about 80% within a particle size range of 45−105 μm could be achieved.

In the GA process, the melt delivery nozzle was subjected to rapid cooling by impacting from the high-speed cold gas flow. Therefore, a higher melting temperature was chosen to prevent melt solidification or clogging in the melt delivery nozzle.

2.2 L-DED process for part preparation

In this study, the L-DED parts were built on ZL104 aluminum substrates from GA powder and RDA powder, respectively, using LMD−8060 equipment from Raycham Co. Ltd. The machine was equipped with a fiber laser operating at (1070±10) nm with a maximum output power of 4000 W. The powders were dried at 80 °C to reduce humidity and residual oxygen content.

Block samples of 15 mm × 15 mm × 15 mm were fabricated by varying laser power, scanning speed, and powder feed rate to determine the processing window. Laser power was tested from 1500 to 2500 W, scanning speed from 6 to 14 mm/s, and powder-feeding-disk (PFD) rotating speed from 0.6 to 1.4 r/min, as listed in Table 1.

The optimal parameters were found to be 2500 W laser power, 14 mm/s scanning speed, and 1.4 r/min PFD rotating speed. These parameters were used to build L-DED parts of 120 mm × 30 mm × 80 mm from the GA and RDA powders, respectively.

2.3 Testing methods of powder and part properties

The chemical composition of GA powder, RDA powder and the as-built parts was determined using standard chemical analysis methods. Silicon (Si) and magnesium (Mg) contents were assessed via inductively coupled plasma optical emission spectrometry (ICP-AES), while oxygen (O) content was measured using inert gas fusion-infrared absorption method.

Table 1 L-DED processing parameters

Laser power/W	Scanning speed/(mm·s^{-1})	Powder feeding rate/(r·min^{-1})	Hatch distance/mm	Layer thickness/mm	Spot size/mm	Scanning strategy	Shielding gas flow/(L·min^{-1})
1500−2500	6−14	0.6−1.4	1.5	0.25	4.0	Zigzag	5

Powder particle morphology was observed under a scanning electron microscope (SEM, Zeiss Merlin) at an acceleration voltage of 5 kV and a probe current of 100 pA. Cross-sections of powder particles were examined using an optical microscope after being polished to 2500#. The granularity and morphology of powder particles were quantified based on an image analysis method using 500NanoXY equipment (Occhio Instruments, Belgium), with over 100000 particles analyzed for each powder at a resolution of 1.129 μm/pixel. Internal defects in powder particles and resulting parts were examined using a micro-focus computed tomography (CT) system at a resolution of 2 μm, acceleration voltage of 90 kV, and a probe current of 90 μA. The porosity of the parts was determined by scanning 2 mm × 2 mm × 2 mm cubes prepared by electro-discharge machining (EDM) wire-cutting. Surface roughness was measured using a KEYENCE laser scan confocal microscope. The relative densities of the parts under different fabrication conditions were determined using the Archimedes drainage method in ethanol. The microstructures of the parts were observed with an optical microscope after being polished to 2500# and etched with Keller's reagent for 10 s. X-ray diffraction patterns were obtained using an XRD diffractometer at 5 (°)/min with an acceleration voltage of 40 kV and an acceleration current of 20 mA. More detailed microstructural information was acquired using a transmission electron microscope (TEM, JEOL® JEM−2100) at an accelerating voltage of 200 kV. Hardness values were measured via a Vickers hardness tester at a force of 49 N. Tensile specimens were fabricated from parts in both vertical (V) and horizontal (H) directions. Uniaxial tensile tests were performed at room temperature on a creep testing machine at a tensile rate of 0.1 mm/min, with four specimens tested for each condition.

3 Results

3.1 Powder characteristics

3.1.1 Chemical composition

The loss rate of element i in the alloy (R_i) can be approximated by the Langmuir equation [22]:

$$R_i(P_i,T)=\frac{P_i}{k_{\mathrm{av}}}\left(\frac{M_i}{2\pi RT}\right)^{0.5} \quad (1)$$

where M_i (g/mol) represents the molecular mass of element i, P_i (Pa) denotes the partial pressure of the saturated vapor of element i, R denotes the molar gas constant (8.31 J/(mol·K)), k_{av} represents the reduced vaporization rate in a vacuum, and T (K) is the thermodynamic temperature of molten metal. Equation (1) indicates that the element loss rate primarily depends on melt temperature and the temperature-dependent saturated vapor pressure of the element. The saturated vapor pressures of Al and Si, far below that of Mg, remain relatively stable at temperature between 800 °C (973.15 K) and 900 °C (1173.15 K). However, the saturated vapor pressure of Mg increases by about 100 times within this temperature range [22]. Therefore, the loss rate of Mg changes rapidly.

The chemical compositions of GA powder and RDA powder are listed in Table 2. Although master alloy ingots from the same batch were used in this experiment, the loss of Mg in the GA process was more severe due to its higher melting temperature, which caused a low Mg content in the GA powder. In comparison, the RDA process allows for continuous preparation of metal powder at a lower melting temperature, significantly reducing the loss of low-melting-point elements, thus allowing for more precise control over the powder composition.

Table 2 Chemical composition of GA and RDA AlSi10Mg powders and as-built parts (wt.%)

Material	Si	Mg	O	Al
GA powder	10.68	0.56	0.027	Bal.
RDA powder	10.46	0.65	0.0088	Bal.
GA part	10.46	0.31	0.008	Bal.
RDA part	10.20	0.43	<0.0005	Bal.

3.1.2 Powder granularity

As shown in Fig. 2, the particle sizes of both powders are mainly distributed between 40 and 105 μm. The average particle size of the RDA powder is larger than that of the GA powder. However, the GA powder has a narrower particle size distribution (PSD), concentrated between 60 and 90 μm, and contains a larger fraction of fine particles than the RDA powder. These qualities enhance the apparent density by packing the gaps between powder particles.

3.1.3 Powder morphology

Figures 3(a) and (b) show that the GA and

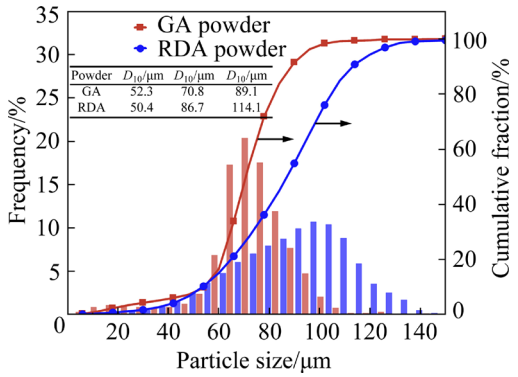

Fig. 2 Particle size distributions of GA and RDA powders

RDA powders are both spherical or nearly spherical. Generally, large particles tend to be irregularly shaped and have satellite particles adhered onto their surface, which is particularly true of the GA powder. Besides, there are a high fraction of satellite particles with a rough surface in the GA powder. It is difficult to improve the morphology and surface quality of the GA powder particles only by adjusting the atomization pressure in a conventional gas atomization process. Very similar morphological features of gas-atomized aluminum alloy powder particles have been reported in the previous studies [12,27].

In contrast, the RDA powder has a smooth surface with minimal presence of satellite particles. In this study, the spray chamber has an inner diameter exceeding 6 m, which is large enough to prevent particles from interacting significantly with the chamber walls, thus resulting in a scarcity of flat particles in the RDA powder. As shown in Fig. 3(b), irregularly shaped particles in the RDA powder are primarily elongated particles, which are formed through the ligament breakup mode during the RDA process. These elongated particles typically have a small aspect ratio defined as the ratio of the minimum Ferret diameter to the maximum Ferret diameter of a particle.

The aspect ratio distributions of powder particles were analyzed. In the RDA powder, the particles with an aspect ratio below 60% account for approximately 25 vol.% while those with an aspect ratio below 90% account for approximately 50 vol.%. Optical micrographs, as shown in Figs. 3(c, d), indicate that both GA powder and RDA powder contain hollow particles with pore shapes that are roughly circular on the cross-section. Notably, the GA powder contains more hollow particles.

The 500NanoXY device was used to operate the image analysis method to gather more detailed information regarding the morphology of each powder. The particle bluntness and outgrowth rate

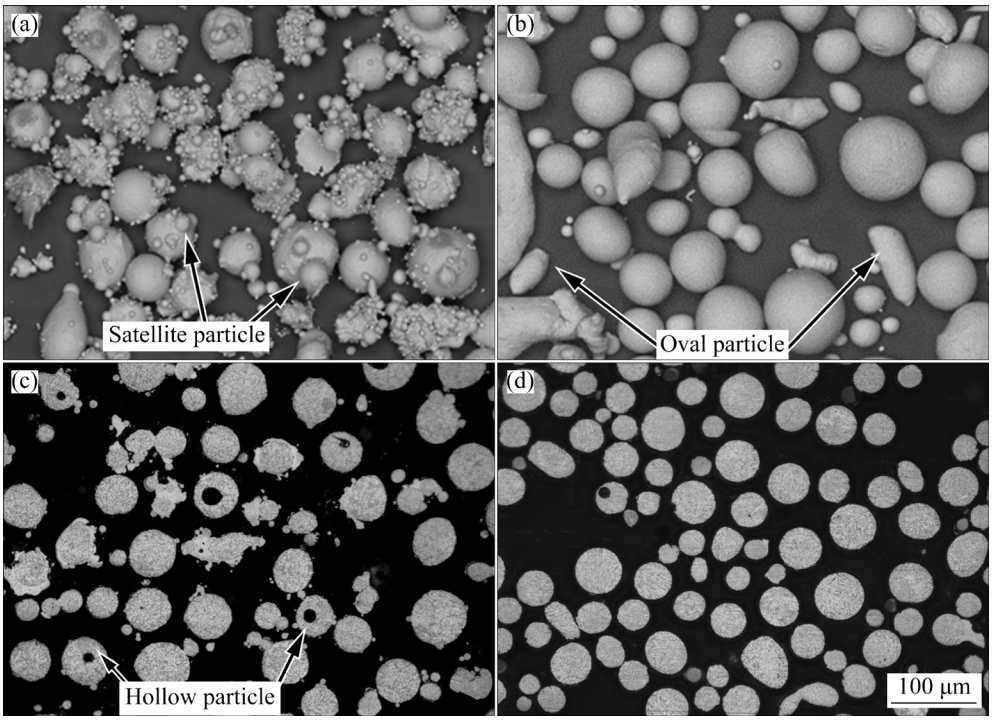

Fig. 3 Particle surface (a, b) and cross-section (c, d) morphologies: (a, c) GA powder; (b, d) RDA powder

were selected to characterize the particle sphericity and the proportion of satellite particles of each powder, respectively. The effects of particle size on these shape parameters were explored.

(1) Bluntness

The particle shape is described here by a 2D parameter called bluntness (W_V) [28], which is expressed as follows:

$$W_V = \frac{1}{\sqrt{\lambda - 1}} \tag{2}$$

$$\lambda = \frac{1}{N}\sum_{i=1}^{i=N}\left(1+\frac{\lambda_E}{\lambda_i}\right)^2 \tag{3}$$

where λ_E represents the radius of the maximum inner tangent circle, while λ_i represents the particle curvature radius at a position i on the particle surface. The bluntness is related to the curvature of particle projection boundary, which is very sensitive to the particle sphericity. A bluntness value of 1 indicates a perfectly spherical particle while a smaller bluntness value indicates a more irregular shape.

As shown in Fig. 4(a), the GA powder predominantly consists of particles with bluntness values between 40% and 60%, accounting for 73.0 vol.%, indicating that most particles have poor sphericity. In the RDA powder, the particles with bluntness values above 90% account for about 50.0 vol.%, indicating that most particles have high sphericity. As shown in Fig. 4(b), both GA powder and RDA powder show a decrease in particle bluntness with an increase in particle size. As the particle size increases from 30 to 110 μm, the bluntness value of the RDA powder decreases from 90% to 80% while that of the GA powder decreases from 60% to 40%.

(2) Outgrowth rate

The outgrowth rate (η) [28] is used here to measure the degree and proportional distribution of satellites:

$$\eta = 1 - \frac{1}{n_{\text{outgrowth}} + 1} \tag{4}$$

where $n_{\text{outgrowth}}$ is the number of satellites attached onto the surface of a large particle. From this equation, the outgrowth rate decreases as fewer satellites are attached onto the surface of a large particle.

As shown in Fig. 5(a), the particles with no satellite adherents (i.e., η=0) account for 45.0 vol.% in the RDA powder particles, versus 3.5 vol.% in the GA powder particles. The particles with two satellites (i.e., η=0.67) occupy 53.1 vol.% in the GA powder particles. As shown in Fig. 5(b), the outgrowth rate of the GA powder remains at a much higher level (η=0.67) with slight fluctuations as the powder particle size increases from 30 to 110 μm, while that of the RDA powder gradually increases from 20% to 51%.

3.1.4 Powder porosity

As shown in Figs. 6(a, b), the porosity of the GA powder particles (1.42%) is approximately four times that of the RDA powder particles (0.35%). These findings are consistent with those by CHEN et al [29] and AHSAN et al [30], who performed comparative studies of GA and PREP Ti6Al4V powders. The RDA process tends to yield powder particles with lower porosity than the GA process. In other words, small voids exist in the RDA powder particles, and those present in the GA powder particles are mainly large ones. For example, the voids with an volume less than 2×10^{-5} mm^3 account for about 75% of total void

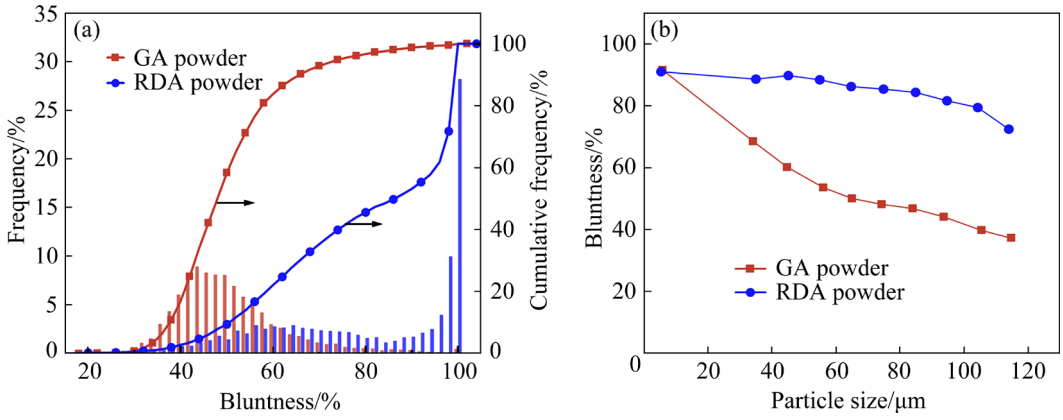

Fig. 4 Bluntness of GA and RDA powders: (a) Bluntness distribution; (b) Bluntness change with particle size

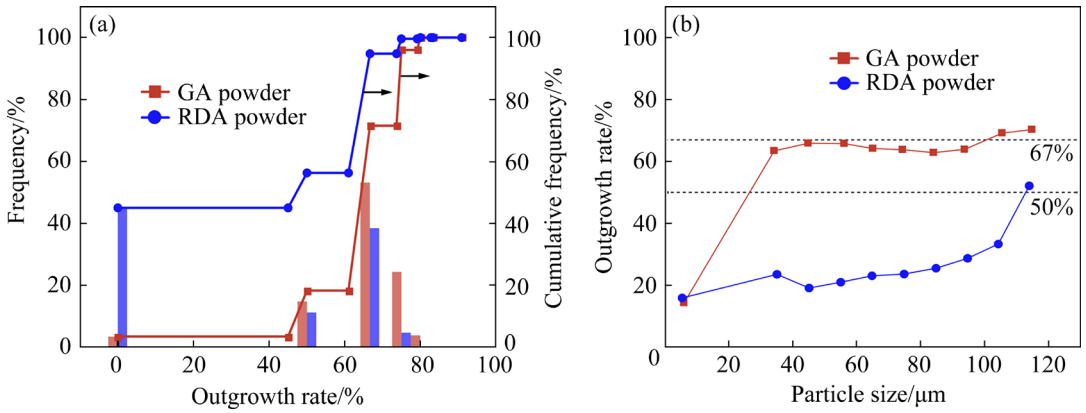

Fig. 5 Outgrowth rate of GA and RDA powders: (a) Outgrowth rate distribution; (b) Outgrowth rate change with particle size

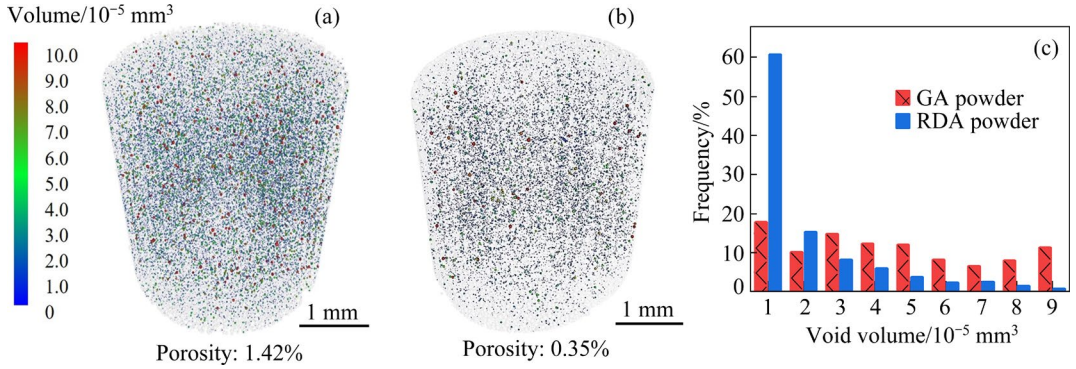

Fig. 6 CT data of AlSi10Mg powders: (a) GA powder; (b) RDA powder; (c) Void volume distribution in powder particles

volume in the RDA powder particles, while in the GA powder particles, the proportion is only 28%, as shown in Fig. 6(c).

3.1.5 Powder flowability and apparent density

As given in Table 3, the RDA powder has superior flowability and apparent density compared to the GA powder. Specifically, it takes for 50 g RDA powder approximately 21 s less than the same amount of GA powder to flow. The remarkable flowability and increased apparent density of the RDA powder contribute to the stability and efficiency of the powder feeding process; these properties improve the quality of as-built parts in the L-DED process.

Table 3 Flowability and apparent density of GA powder and RDA powder

Powder	Flowability for 50 g powder/s	Apparent density/ ($g \cdot cm^{-3}$)
GA	60.21±0.04	1.128±0.005
RDA	38.78±0.58	1.471±0.003

3.1.6 Powder feeding rate

The feeding rates for each powder were calculated by measuring the cumulative mass of powder output in 3 min under different powder-feeding-disk (PFD) rotating speeds. As shown in Fig. 7, there is a clear linear relationship between the powder feeding rate and PFD rotating speed at

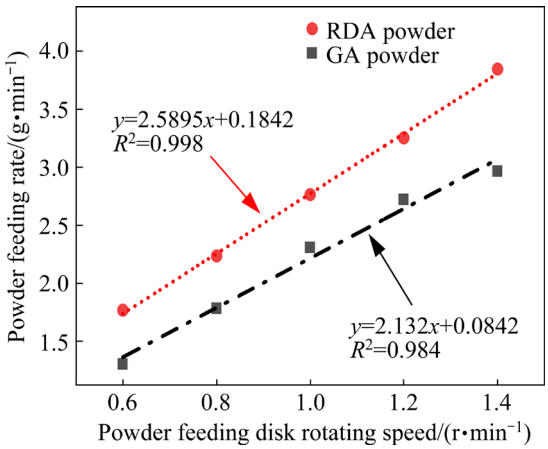

Fig. 7 Variations of powder feeding rate with powder feeding disk rotating speed

speeds slower than 1.4 r/min for both powders, which ensures that both powders could be fed steadily in the experiment. However, the RDA powder indicates higher and more stable powder feeding rates under the same conditions, compared to the GA powder, especially at higher PFD rotating speeds, which would effectively guarantee ultra-high-speed printing using the RDA powder.

3.2 3D printing performance of powders

3.2.1 Printing process window

With the premise of a constant powder mass per unit length, the printing process windows of both GA powder and RDA powder in the L-DED process were investigated based on characteristics analysis of a series of block samples of 15 mm × 15 mm × 15 mm. The samples were fabricated by varying laser power and scanning speed under a constant PFD rotating speed of 1.4 r/min. The maximum density of as-built blocks from each powder was selected as the reference density to calculate the relative density of the specimens. The reference density is 2.657 g/cm^3 for the as-built GA parts, and 2.644 g/cm^3 for the as-built RDA parts, respectively. The printing process window was determined based on a relative density of over 99.5%.

As shown in Fig. 8(a), the printing process window for the GA powder is observed mainly in two regions: Low power and scanning speed (power: 1500−1700 W, scanning speed: 6−8 mm/s), and high power and high scanning speed (power: 2400−2500 W, scanning speed: 6−14 mm/s). Notably, the printing process window of the GA powder is discontinuous. In contrast, the printing process window of the RDA powder is considerably larger, with the exceptions of extreme conditions of low power and high scanning speed (power: 1500−2000 W, scanning speed: 8−14 mm/s).

3.2.2 Printing quality of L-DED parts

Based on the information shown in Fig. 8, the optimal printing parameters were identified for a comparative analysis of the 3D printing performance in the L-DED process using both powders. The selected parameters were laser power 2500 W, scanning speed 14 mm/s, and PFD rotating speed 1.4 r/min. The L-DED parts with designed dimensions of 120 mm × 30 mm × 80 mm were fabricated from GA powder and RDA powder, respectively, as shown in Fig. 9. The surface roughness of the as-built GA part is (220±40) μm, while that of the as-built RDA part is (160±20) μm, indicating that the latter has better surface quality.

Dimensional accuracy, which describes the deviation of the actual dimensions from the designed dimensions of a part, was assessed by measuring the average values of length, width, and height at five sections of each as-built part. The as-built GA part shows deviations of (2.5±0.8)% in length, (20.0±7.1)% in width, and (2.5±2.5)% in height. In contrast, the as-built RDA part shows deviations of (1.7±0.8)% in length, (13.0±6.2)% in width, and (1.3±1.2)% in height. Therefore, the as-built RDA part has a higher dimensional accuracy than the as-built GA part.

Black smoke and powder splashing are observed during the L-DED process of the GA powder, which causes poor surface quality and low

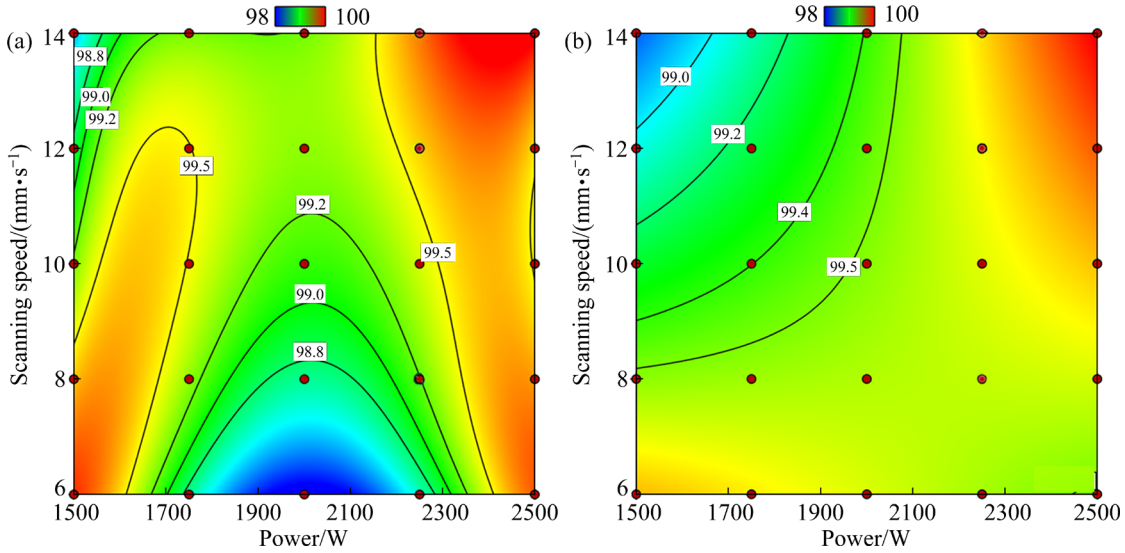

Fig. 8 Relative density distribution of as-built L-DED parts: (a) From GA powder; (b) From RDA powder

dimensional accuracy of the as-built part. Conversely, the L-DED process of the RDA powder shows minimal black smoke and powder splashing, ensuring a smooth surface and high dimensional accuracy of the as-built part.

Figure 10 shows the porosity and void volume distribution in the as-built L-DED parts. The porosity is about 1.01% in the as-built GA part, against 0.67% in the as-built RDA part. As described by NG et al [31], L-DED with gas-assisted powder transfer is associated with two types of porosity: lack-of-fusion and gas porosity. In this study, both as-built L-DED parts were prepared under the same optimized process conditions, and lack-of-fusion is minimal. Instead, the gas porosity dominates in both as-built L-DED parts.

During the L-DED process, some trapped gas escapes from the powder as it melts while some ambient gas is trapped in the melt pool. The competition between these two processes determines the gas porosity in the final as-built parts. However, tracking the gas escaping from the molten powder is very challenging. Compared with the virgin powders, the porosity in the as-built GA part (1.01%) is lower than that in the GA powder (1.41%), as reported by NG et al [31]. The porosity in the as-built RDA part (0.67%) is higher than that in the RDA powder (0.35%). This suggests that more trapped gas escapes from the GA powder during melting, while the melt pool of the RDA powder retains more ambient gas. Additionally, as depicted in Fig. 10(c), the large voids with the volume exceeding 50×10^{-5} mm^3 are present in the as-built GA part (accounting for about 5% of total void volume) but are scarce in the as-built RDA part.

3.2.3 Microstructure of L-DED parts

As shown in Figs. 11(a, c), both as-built parts predominantly consist of α(Al) phase (white) and eutectic Si phase (gray). Coarse Si precipitates are distributed around the α(Al) matrix in both as-built parts. However, significant changes in the microstructures of both heat-treated parts occur after the T6 heat treatment (quenching after solid solution at 525 °C for 60 min, followed by aging at180 °C for 480 min), as shown in Figs. 11(b, d). After the solution treatment, most of coarse eutectic

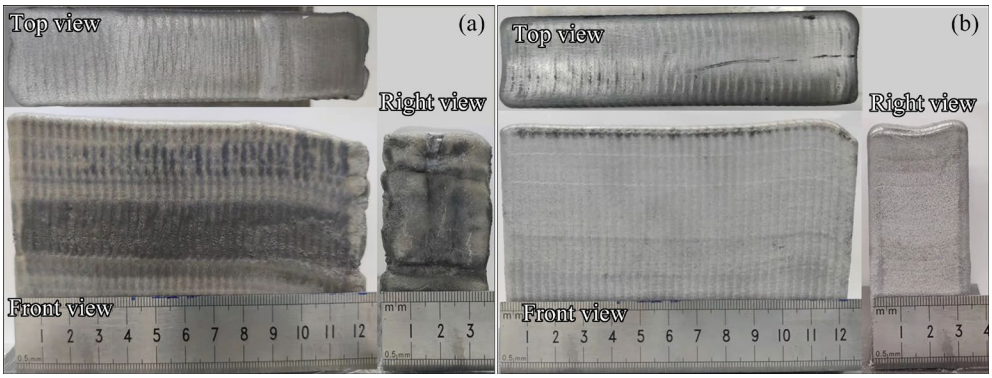

Fig. 9 Dimensions of as-built parts: (a) From GA powder; (b) From RDA powder

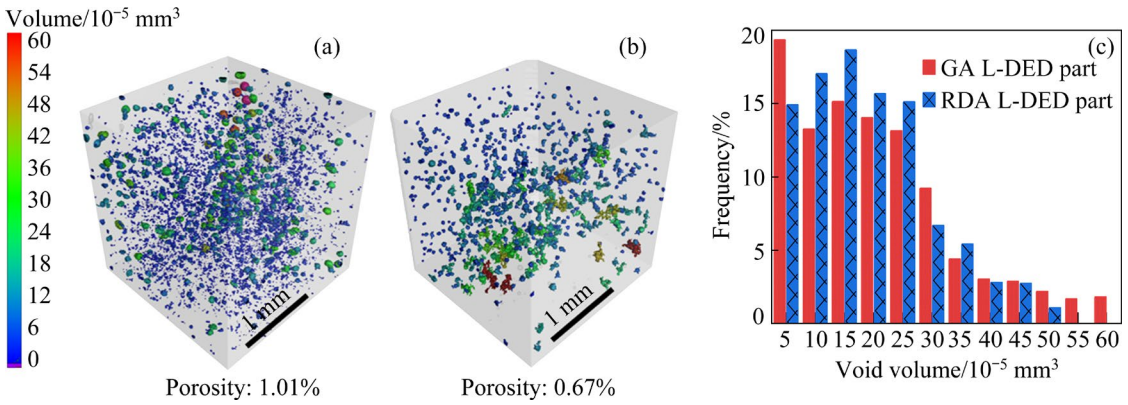

Fig. 10 CT data of AlSi10Mg as-built parts: (a) From GA powder; (b) From RDA powder; (c) Void volume distribution in L-DED parts

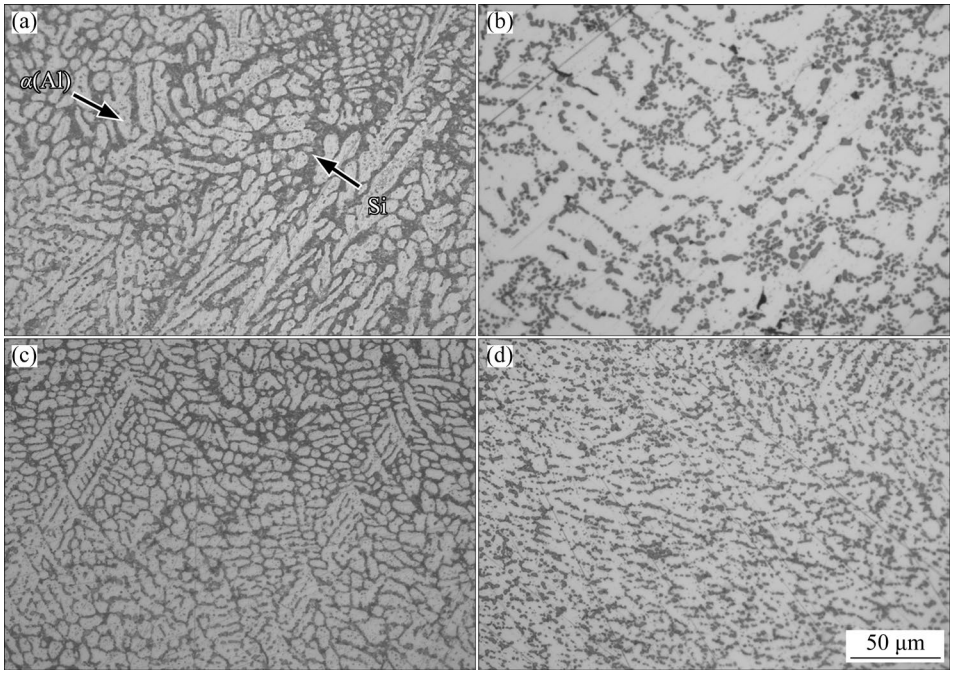

Fig. 11 Microstructures of L-DED parts printed using two kinds of powders: (a) As-built GA part; (b) Heat-treated GA part; (c) As-built RDA part; (d) Heat-treated RDA part

Si phase dissolves and re-solidifies into the α(Al) matrix, while a portion of coarse Si phase transforms into small Si particles. During the subsequent aging treatment, these solidified Si particles precipitate and redistribute in the matrix. Comparatively, under both as-built and heat-treated conditions, the Si precipitates in the RDA parts are finer and more uniformly distributed than those in the GA parts.

As shown in Fig. 12, the XRD results indicate that the two virgin AlSi10Mg powders and as-built parts consist mainly of α(Al) matrix and eutectic Si phase. Detecting Mg_2Si phase by XRD is challenging due to its low content in both as-built parts. However, weak Mg_2Si diffraction peaks are detected after the T6 heat treatment in both heat-treated parts, confirming the increased precipitation of Mg_2Si phase during the treatment. The Mg_2Si phase peaks of the heat-treated RDA parts are more pronounced compared to those of the heat-treated GA parts, indicating a higher precipitation of Mg_2Si phase in the former.

The composition of the heat-treated parts was analyzed using transmission EDS, as depicted in Figs. 13(a, b). The contents of the matrix elements based on EDS analysis are consistent with the testing results in Table 2. Those small particles, measuring approximately several tens of nano-meter

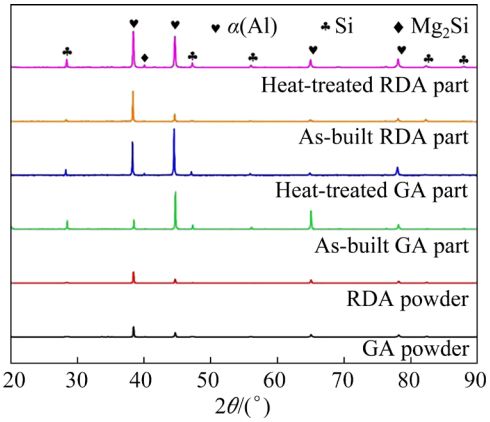

Fig. 12 XRD patterns of GA and RDA powders and corresponding printed parts under as-built and heat-treated conditions

and exhibiting a Mg/Si mass ratio close to 1.73, can be inferred as the precipitated Mg_2Si phase. Notably, Fig. 13(a) also reveals the presence of fine Si particles. Furthermore, a higher precipitation of Mg_2Si phase is observed in the heat-treated RDA parts, which is in line with the XRD results in Fig. 12.

3.2.4 Mechanical properties of L-DED parts

Table 4 summarizes the mechanical properties of L-DED parts, including hardness, ultimate tensile strength (UTS), yield strength (YS, $R_{p0.2}$), and elongation. The engineering stress−strain curves of the horizontally loaded specimens are

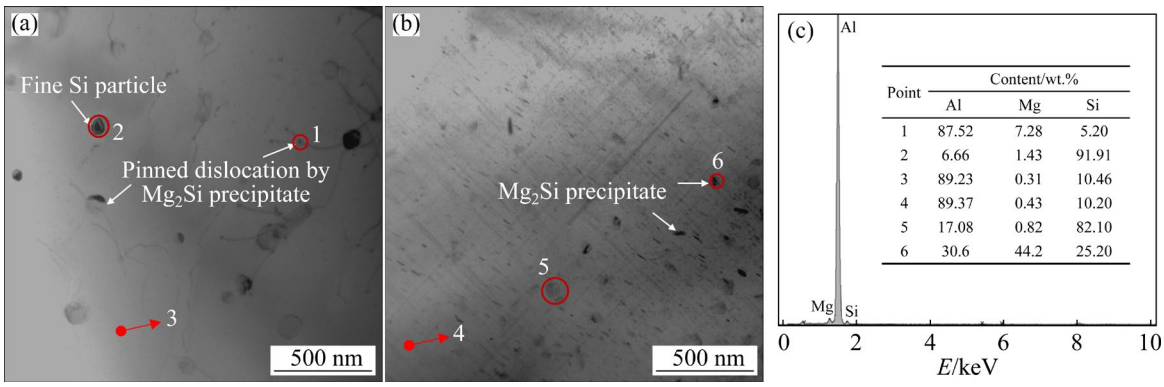

Fig. 13 Microstructures and EDS spectra of two kinds of heat-treated L-DED parts: (a) GA; (b) RDA; (c) EDS spectra

Table 4 Mechanical properties of AlSi10Mg components fabricated from GA and RDA powders

Specimen	As-built				Heat-treated			
	Hardness ($HV_{0.5}$)	UTS/MPa	YS/MPa	Elongation/%	Hardness ($HV_{0.5}$)	UTS/MPa	YS/MPa	Elongation/%
GA-H	72 ± 5	141±3	88±2	16.6±1.2	109 ± 4	288 ± 2	250±2	6.2±0.5
GA-V		133±4	70±3	16.0±1.2		252 ± 9	220±3	6.1±1.2
RDA-H	82 ± 4	181±1	100±1	15.8±0.8	124 ± 3	356 ± 5	318±2	6.3±1.2
RDA-V		167±3	94±3	14.7±2.0		334 ± 5	286±4	5.8±1.5

GA-H: Horizontally loaded GA specimen; GA-V: Vertically loaded GA specimen; RDA-H: Horizontally loaded RDA specimen; RDA-V: Vertically loaded RDA specimen

shown in Fig. 14. The UTS values of the RDA specimens are higher than those of the GA specimens in both as-built and heat-treated states, albeit with slightly lower plasticity. Additionally, the UTS values of the specimens perpendicular to the building direction are higher than those along the building direction.

The UTS values of the heat-treated specimens increase significantly in comparison to the as-built ones, but the plasticity decreases. After the treatment, the UTS values of the horizontally loaded GA specimens increase from (141±3) to (288±2) MPa while those of the horizontally loaded RDA specimens increase from (181±1) to (356±3) MPa. The optimal UTS of the RDA parts is slightly higher than that reported in the previous studies (as-built: 181 MPa here vs 170 MPa [32], heat-treated: 356 MPa here vs 340 MPa [33]). Those L-DED parts in Refs. [32,33] were fabricated from GA powders, but by different L-DED machines. The L-DED parts in Ref. [32] were produced under laser power of 2000 W, scanning speed of 5 mm/s, and powder feed rate of 2.4 g/min, approximately corresponding to the powder feed rate of 0.8 r/min used in the present work. The

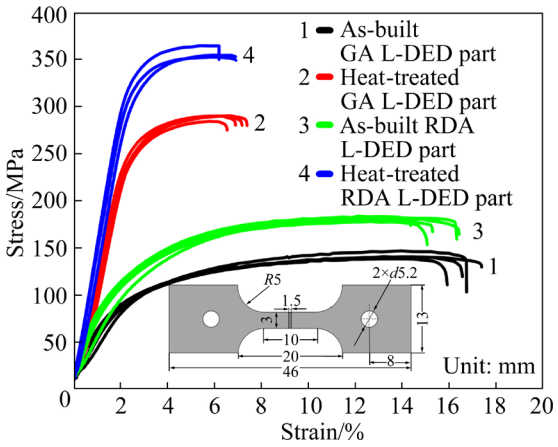

Fig. 14 Engineering stress−strain curves for GA and RDA L-DED parts under as-built and heat-treated conditions

L-DED parts in Ref. [33] were built under laser power of 3000 W, scanning speed of 12 mm/s, and powder feed rotation speed of 2 r/min.

As shown in Fig. 15, the fractures are densely covered with dimples in both as-built and heat-treated specimens, indicating ductile fractures. No obvious defects such as porosity or unmelted powder particles are found on the fractures, confirming that both the GA specimens and RDA

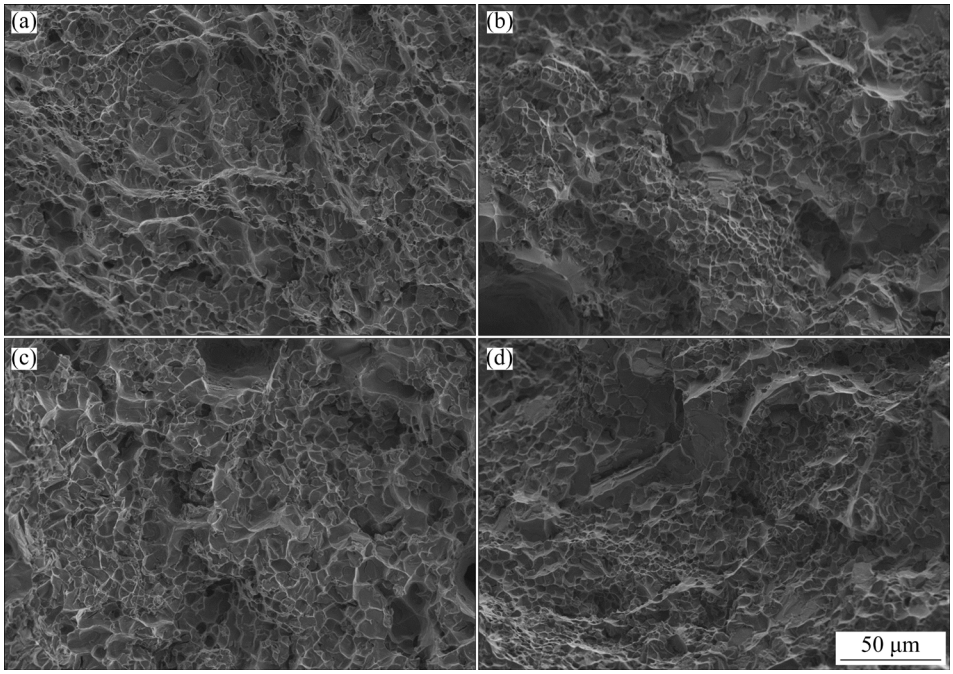

Fig. 15 Fracture morphologies of GA and RDA specimens under as-built and heat-treated conditions: (a) As-built GA specimens; (b) Heat-treated GA specimens; (c) As-built RDA specimens; (d) Heat-treated RDA specimens

specimens are of favorable printing quality. After heat treatment, both GA specimens and RDA specimens show a significant reduction in the number of dimples on the fractures, indicating a decrease in plasticity.

4 Discussion

4.1 Effect of atomization method on powder characteristics

4.1.1 Powder morphology

The morphology of powder particles is mainly determined by spheroidization time and solidification time of atomized droplets. The spheroidization time (τ_{sph}) is described by the following empirical correlation [34]:

$$\tau_{sph}=\frac{3\pi^2\mu_L}{4V\sigma}\cdot\left(\frac{1}{2}\right)^4\left(d_1^4-d_2^4\right) \quad (5)$$

where d_1 and d_2 are the droplet diameter after spheroidization and the minimum diameter before spheroidization, respectively; μ_L is the melt viscosity, V is the droplet volume, and σ is the melt surface tension.

According to Eq. (5), the spheroidization time depends on the droplet viscosity, volume, diameter, and surface tension. By assuming constant melt viscosity and surface tension, smaller droplets tend to spheroidize more easily. This explains the decrease in sphericity of both GA and RDA powder particles with increasing particle size (Figs. 3 and 4). However, more irregularly shaped particles are observed in the GA powder (Fig. 3), which may be attributed to higher solidification rates. The GA process has been reported to exhibit higher droplet cooling rates of 10^4−10^6 K/s [35] compared to 10^3−10^5 K/s in the RDA process [36]. A higher cooling rate results in a higher solidification rate. Consequently, droplets in the GA process tend to have higher solidification rates than those of the same size in the RDA process. This disparity often leads to insufficient droplet spheroidization in the GA process, as droplet solidification time can be shorter than the spheroidization time, leading to the formation of non-spherical powder particles. Further, the relatively high oxygen content in the gas-atomized metallic droplets enhances the irregularity of the GA powder particles.

4.1.2 Satellite particles

The presence of satellite particles can be attributed to the collisions between large droplets and small particles/droplets during the spray process [12,37]. In the GA process, a gas/droplet recirculation region is typically formed between the gas/droplet spray and the spray chamber wall in a bounded spray chamber [38], as shown in Fig. 16.

Within this gas/droplet recirculation region, numerous fine droplets/particles are often found due to their low inertia. These particles cool down and solidify as they move upward, potentially entering the upstream region of the spray as fine solid particles. Thus, frequent collisions among droplets/particles occur. The gas-atomized droplets/particles in the GA process also exhibit a wide size distribution, and their motion states change significantly in a turbulent gas flow field, further increasing the frequency of droplet/particle collisions in the spray region.

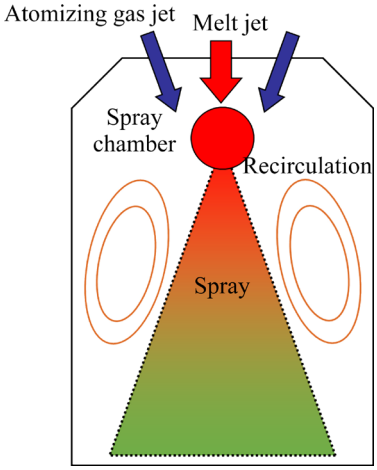

Fig. 16 Schematic diagram of gas/droplet recirculation in spray chamber during GA process

In contrast, the formation of such a gas/droplet recirculation region in the GA process can be avoided in the RDA process. Droplets in the RDA process typically have a more uniform size distribution and follow similar trajectories, significantly reducing the droplet/particle collision frequency. Therefore, compared to the GA process, the RDA process produces much fewer satellite particles (Figs. 3 and 5).

4.1.3 Hollow particles

Insoluble gas entrapped in solidified droplets leads to the formation of hollow particles. During the GA process, the strong gas shear on the melt film can entrap gas into the melt, which subsequently disintegrates into droplets containing bubbles, forming hollow particles after the solidification [39,40]. The formation of hollow particles is also considered to be potentially related to the breaking apart and closure of membranous droplets during secondary atomization [41]. The breakup modes of a full liquid droplet can be classified by the gas Weber number (*We*):

$$We=\frac{\rho_{\mathrm{g}}U_{\mathrm{rel}}^{2}D_{\mathrm{d}}}{\sigma} \tag{6}$$

where ρ_{g} is the gas density, U_{rel} is the gas-droplet relative velocity, and D_{d} is the initial droplet diameter. This dimensionless number represents the ratio of the disrupting aerodynamic force to the restorative surface tension force.

The membranous droplet breakup modes, including bag breakup ($12<We\leq50$) and bag-and-stamen breakup ($50<We\leq100$), occur when $12<We<100$ [41,42]. However, due to rapid cooling and solidification during spray process, the droplet breakup process can be interrupted, resulting in gas being enclosed within the bag or umbrella structure, as shown in Fig. 17. In the GA process, the gas−droplet relative velocity often exceeds several hundred meters per second in the atomization zone [43,44], so the *We* value can easily reach the condition of $We>12$. As a result, membranous droplet breakup modes are commonly observed during second atomization process [45], thereby enhancing the hollow particle formation. A strong turbulent multiphase flow field in the GA process also promotes collision and merging among droplets, thus increasing the probability of gas entrapment within droplets.

In the RDA process, the melt is atomized into droplets, ligaments, or sheets at the edge of rotating disk due to centrifugal force [46]. These primary fragments, once they leave the rotating disk, are subjected to aerodynamic force in spray chamber, which is not as strong as in the GA process. In this study, a flat disk with a diameter of 30 mm was employed with a rotating speed of 30000 r/min in the RDA process. Under these conditions, the gas Weber number (*We*) is on a level of 10^{-1}–10^{0}, which cannot meet the onset of membranous droplet breakup modes, thus decreasing the probability of hollow particle formation.

4.1.4 Powder flowability and apparent density

Both powder granularity and morphology can affect powder flowability and apparent density. In general, a suitable proportion of fine particles can fill the gaps among larger particles and lubricate them, thereby increasing powder apparent density and flowability [47]. However, in this study, the apparent density and flowability of the GA powder

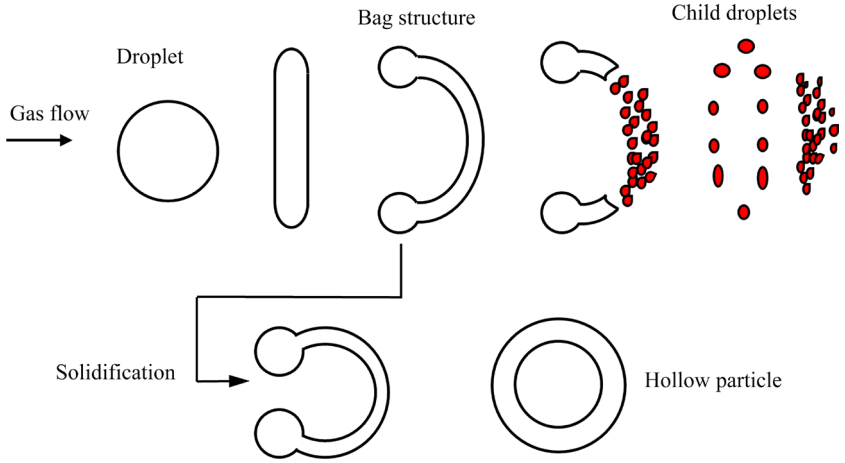

Fig. 17 Schematic diagram of membranous droplet breakup mode and hollow particle formation mechanism

are poorer than those of the RDA powder. According to MELLMANN et al [48], the powder flow properties are strongly influenced by the particle shape. As particles deviate from a spherical shape and particle surface roughness increases, the powder flow properties degrade. A higher fraction of irregular particles and satellite particles in the GA powder may have resulted in larger gaps among the particles, thereby reducing powder apparent density and flowability during the packing process. Moreover, the friction among the particles significantly influences the powder packing and flowing behaviors. The friction becomes more pronounced when particles are smaller in size [47]. The GA powder contains a much higher fraction of fine and irregular particles, which may have been detrimental to its flowability and apparent density.

4.2 Effect of atomization method on powder printability

4.2.1 Melt pool stability analysis

The L-DED process is a rapid non-equilibrium metallurgical process characterized by fast melting and cooling rates (10^3−10^6 K/s) [33,49]. The stability of melt pool plays a crucial role in achieving a uniform local temperature distribution and the desired microstructures in as-built parts [17,50−52].

Fluctuations in melt pool are closely related to powder flow, which is influenced by factors such as powder feeding rate, velocity of particles entering melt pool, and spatial spread of powder flow out of the deposition nozzle [53]. In the L-DED process, the powder is transported by an inert gas flow from powder feeding disk to coaxial powder outlet. The GA powder has a lower and less stable powder feeding rate, as shown in Fig. 7. Large fluctuations in the number of particles entering melt pool readily destabilize melt pool shape and size [54]. The RDA powder enables more efficient and stable powder feeding into melt pool, thereby maintaining the stability of the melt pool during the L-DED process.

In-flight particles in the powder flow can interact with the laser beam, partially blocking the laser. This interaction can cause particles to melt or vaporize before they enter melt pool, creating pressure gradients at particle surface. These surface pressure gradients accelerate the force propelling particles towards the melt pool, thus intensifying fluctuations in the melt pool [53]. It is reasonable to assume that this phenomenon is more pronounced for the GA powder, as it contains a higher concentration of satellites or sub-sized particles on its surface. The presence of more hollow particles in the GA powder can also contribute to bursting in the melt pool and enhance gas entrapment in the material [31]. In addition, the presence of higher oxygen content in the GA powder may also promote the spattering and oxidation during the L-DED process.

Further investigation is required to thoroughly understand the impact of powder morphology on powder flow and the interaction mechanism between impacting particles and the melt pool. This could be achieved through numerical simulations and in-situ observation methods.

4.2.2 Microstructure and mechanical properties

As shown in Figs. 11(a, c), the deposited aluminum alloy specimens have coarse Si precipitates surrounding the α(Al) matrix. The

as-built parts display a uniform microstructure, which can be attributed to the interaction between the phase transformation behavior of AlSi10Mg and the non-equilibrium nature of the L-DED process. The rapid cooling rate associated with the L-DED process increases the solubility of Si in the Al matrix [54], which can transform the coarse primary Si precipitates into dispersed fine eutectic Si particles. However, repeated remelting and solidification cause severe heat accumulation in underlying layers, thus reducing the cooling rate and promoting the precipitation and growth of eutectic Si phase.

The poor quality of the GA powder results in excessive black smoke and spattering during the printing process, adversely affecting the surface and dimensional accuracy of the as-built part. Large fluctuations in melt pool also create variations in the local thermal histories, resulting in a coarser and more uneven microstructure in the as-built GA part. In contrast, the as-built RDA part has a finer and more uniform microstructure due to minimal melt pool fluctuations during the printing process.

As shown in Figs. 11(b, d), both the L-DED parts become finer and more uniform after the T6 heat treatment. The treatment promotes the solid solution of Mg and Si, thus providing a more uniform supersaturated solid-solution Al alloy. Subsequent artificial aging facilitates the precipitation of Mg_2Si phase, as shown in Fig. 12. In Fig. 13, it is observed that the dislocations are pinned by the fine Mg_2Si precipitates. Previous studies [55,56] have shown that, despite the low content of Mg_2Si, its pinning effect on the dislocation significantly enhances the strength of the parts. Given the higher Mg content in the RDA part, a larger amount of Mg_2Si phase precipitates after heat treatment, enhancing the second phase strengthening of the matrix. The heat-treated RDA specimens show higher strength than the heat-treated GA specimens overall due to their more uniform microstructures and the strengthening effect of their abundant Mg_2Si precipitates.

The weakest point of an L-DED part is the junction between upper and lower layers, which translates into higher UTS values of the GA and RDA specimens perpendicular to the building direction compared to those along the building direction.

5 Conclusions

(1) There are significant differences between GA and RDA aluminum alloy powders. In the preferred particle size range (40−105 μm) for the L-DED process, the GA powder has a narrower PSD and a higher volume fraction of fine particles than the RDA powder. However, the GA powder shows inferior overall performance due to the lower sphericity, higher proportion of satellite particles and hollow particles, reduced flowability, and lower apparent density.

(2) In comparison to the GA powder, the RDA powder demonstrates superior adaptability to variations in laser power and scanning speed, owing to its exceptional overall performance. Additionally, the RDA powder provides a relatively wide printing process window, allowing for greater flexibility in printing parameters.

(3) With optimal printing process parameters, the L-DED parts fabricated from the RDA powder show higher dimensional accuracy, while those from the GA powder show some localized collapsed edges.

(4) The ultimate tensile strength of the RDA L-DED parts surpasses that of the GA L-DED parts in both as-built and heat-treated states due to a more homogeneous and finer microstructure. The significant increase in strength is attributed to the formation of numerous Mg_2Si precipitates after the T6 heat treatment, resulting in a UTS value of (356±5) MPa for the RDA L-DED parts.

CRediT authorship contribution statement

Gang RUAN: Methodology, Investigation, Data Curation, Writing − Original draft; **Yu-dong LIANG**, **Gan LI** and **Ying JIN:** Investigation, Data curation; **Xing-gang LI:** Term, Conceptualization, Writing − Review & editing, Supervision, Project administration, Funding acquisition.

Declaration of competing interest

The authors declare that they have no known competing financial interests or personal relationships that could have appeared to influence the work reported in this paper.

Data Availability

The raw/processed data required to reproduce these findings of this study are available from the corresponding author upon request.

Acknowledgments

This work was supported by the National Natural Science Foundation of China (No. 52074157), Department of Education of Guangdong Province, China (No. 2023KTSCX121), and Shenzhen Science and Technology Programs, China (Nos. JSGG20210802154210032, JCYJ20210324104608023, JSGG20180508152608855). The authors would also like to acknowledge the technical support from Southern University of Science and Technology Core Research Facilities, China.

References

[1] STOJANOVIC B, BUKVIC M, EPLER I. Application of aluminum and aluminum alloys in engineering [J]. Applied Engineering Letters : Journal of Engineering and Applied Sciences, 2018, 3(2): 52−62. https://doi.org/10.18485/aeletters.2018.3.2.2.

[2] KOTADIA H R, GIBBONS G, DAS A, HOWES P D. A review of laser powder bed fusion additive manufacturing of aluminium alloys: Microstructure and properties [J]. Additive Manufacturing, 2021, 46: 102155. https://doi.org/10.1016/j.addma.2021.102155.

[3] ABOULKHAIR N T, MASKERY I, TUCK C, ASHCROFT I, EVERITT N M. Improving the fatigue behaviour of a selectively laser melted aluminium alloy: Influence of heat treatment and surface quality [J]. Materials & Design, 2016, 104: 174−182. https://doi.org/10.1016/j.matdes.2016.05.041.

[4] DEBROY T, WEI H L, ZUBACK J S, MUKHERJEE T, ELMERJ J W, MILEWSKI O, BEESEA A M, WILSON-HEID A D, ZHANG W. Additive manufacturing of metallic components – Process, structure and properties [J]. Progress in Materials Science, 2018, 92: 112−224. https://doi.org/10.1016/J.PMATSCI.2017.10.001.

[5] TAMMAS-WILLIAMS S, TODD I. Design for additive manufacturing with site-specific properties in metals and alloys [J]. Scripta Materialia, 2017, 135: 105−110. https://doi.org/10.1016/J.SCRIPTAMAT.2016.10.030.

[6] PANWISAWAS C, TANG Y T, REED R C. Metal 3D printing as a disruptive technology for superalloys [J]. Nature Communications, 2020, 11: 2327. https://doi.org/10.1038/s41467-020-16188-7.

[7] ABOULKHAIR N T, SIMONELLI M, PARRY L, ASHCROFT I, TUCK C, HAGUE R. 3D printing of Aluminium alloys: Additive Manufacturing of Aluminium alloys using selective laser melting [J]. Progress in Materials Science, 2019, 106: 100578. https://doi.org/10.1016/j.pmatsci.2019.100578.

[8] BEESE A M, CARROLL B E. Review of mechanical properties of Ti−6Al−4V made by laser-based additive manufacturing using powder feedstock [J]. JOM, 2015, 68(3): 724−734. https://doi.org/10.1007/S11837-015-1759-Z.

[9] VOCK S, KLÖDEN B, KIRCHNER A, WEIßGÄRBER T, KIEBACK B. Powders for powder bed fusion: A review [J]. Progress in Additive Manufacturing, 2019, 4(4): 383−397. https://doi.org/10.1007/s40964-019-00078-6.

[10] ZHONG Chong-liang, CHEN Jing, LINNENBRINK S, GASSER A, SUI S, POPRAWE R. A comparative study of Inconel 718 formed by high deposition rate laser metal deposition with GA powder and PREP powder [J]. Materials & Design, 2016, 107: 386−392. https://doi.org/10.1016/j.matdes.2016.06.037.

[11] BAJAJ P, HARIHARAN A, KINI A, KÜRNSTEINER P, RAABEE D, JÄGLE A. Steels in additive manufacturing: A review of their microstructure and properties [J]. Materials Science and Engineering A, 2020, 772: 138633. https://doi.org/10.1016/J.MSEA.2019.138633.

[12] LI Xing-gang, ZHU Qiang, SHU Shi, FAN Jian-zhong, ZHANG Shao-ming. Fine spherical powder production during gas atomization of pressurized melts through melt nozzles with a small inner diameter [J]. Powder Technology, 2019, 356: 759−768. https://doi.org/10.1016/j.powtec.2019.09.023.

[13] ZHANG Li-chong, XU Wen-yong, LI Zhou, ZHENG Liang, LIU Yu-feng, ZHANG Guo-qing. Characterization of particle shape of nickel-based superalloy powders using image processing techniques [J]. Powder Technology, 2022, 395: 787−801. https://doi.org/10.1016/j.powtec.2021.10.013.

[14] TAMMAS-WILLIAMS S, WITHERS P J, TODD I, PRANGNELL P B. Porosity regrowth during heat treatment of hot isostatically pressed additively manufactured titanium components [J]. Scripta Materialia, 2016, 122: 72−76. https://doi.org/https://doi.org/10.1016/j.scriptamat.2016.05.002.

[15] PEGUES J W, SHAO S, SHAMSAEI N, SANAEI N, FATEMI A, WARNER D H, LI P, PHAN N. Fatigue of additive manufactured Ti−6Al−4V, Part I: The effects of powder feedstock, manufacturing, and post-process conditions on the resulting microstructure and defects [J]. International Journal of Fatigue, 2020, 132: 105358. https://doi.org/10.1016/J.IJFATIGUE.2019.105358.

[16] ANDERSON I E, WHITE E M H, DEHOFF R. Feedstock powder processing research needs for additive manufacturing development [J]. Current Opinion in Solid State and Materials Science, 2018, 22(1): 8−15. https://doi.org/10.1016/j.cossms.2018.01.002.

[17] SAHEB S H, DURGAM V K, CHANDRASHEKHAR A. A review on metal powders in additive manufacturing [C]// The Third International Conference on Inventive Material Science Applications. Icima, 2020. https://doi.org/10.1063/5.0026203.

[18] RUAN Gang, LIU Chang, QU Hong-qiao, GUO Chuan, LI Gan, LI Xing-gang, ZHU Qiang. A comparative study on laser powder bed fusion of In718 powder produced by gas atomization and plasma rotating electrode process [J]. Materials Science and Engineering A, 2022, 850: 143589. 2022. https://doi.org/10.1016/j.msea.2022.143589.

[19] NIE Yan, TANG Jun-jie, HUANG Jun-fei, YU Shu, LI Yun-ping. A study on internal defects of prep metallic powders by using X-ray computed tomography [J]. Materials, 2021, 14(5): 1177. https://doi.org/10.3390/ma14051177.

[20] GUO Rui-peng, XU Lei, ZONG Bernie Ya-ping, YANG Rui. Characterization of prealloyed Ti−6Al−4V powders from EIGA and PREP process and mechanical properties of HIPed powder compacts [J]. Acta Metallurgica Sinica (English

Letters), 2017, 30(8): 735−744. https://doi.org/10.1007/S40195-017-0540-4/FIGURES/11.

[21] LIU Yang, ZHAO Xiao-hao, LAI Yun-jin, WANG Qing-xiang, LEI Li-ming, LIANG Shu-jin. A brief introduction to the selective laser melting of Ti6Al4V powders by supreme-speed plasma rotating electrode process [J]. Progress in Natural Science: Materials International, 2020, 30(1): 94−99. https://doi.org/10.1016/J.PNSC.2019.12.004.

[22] LI Gan, LI Xin-wei, GUO Chuan, ZHOU Yang, TAN Qi-yang, QU Wen-ying, LI Xing-gang, HU Xiao-gang, ZHANG Ming-xing, ZHU Qiang. Investigation into the effect of energy density on densification, surface roughness and loss of alloying elements of 7075 aluminium alloy processed by laser powder bed fusion [J]. Optics & Laser Technology, 2022, 147: 107621. https://doi.org/10.1016/J.OPTLASTEC.2021.107621.

[23] PHAIROTE P, PLOOKPHOL T, WISUTMETHANGOON S. Design and development of a centrifugal atomizer for producing zinc metal powder [J]. International Journal of Applied Physics and Mathematics, 2012: 77−82.

[24] WOLF S, RIEDEMANN T M, BARCLAY J, HOLLADAY JAMIE, ANDERSON I E, CUI Jun. Synthesis and magnetic performance of gadolinium powder produced with rotating disk atomization [J]. Powder Technology, 2020, 359: 331−336. https://doi.org/10.1016/J.POWTEC.2019.09.035.

[25] PLOOKPHOL T, WISUTMETHANGOON S, GONSRANG S. Influence of process parameters on SAC305 lead-free solder powder produced by centrifugal atomization [J]. Powder Technology, 2011, 214: 506−512. https://doi.org/10.1016/J.POWTEC.2011.09.015.

[26] Centrifugal Atomization Powder Production Equipment [EB/OL]. 2024−03−24. http://www.skylinesmt.com/en-US/xjflblsczb/320.html (accessed March 24, 2022).

[27] ASGARI H, BAXTER C, HOSSEINKHANI K, MOHAMMADI M. On microstructure and mechanical properties of additively manufactured AlSi10Mg_200C using recycled powder [J]. Materials Science and Engineering A, 2017, 707: 148−158. https://doi.org/10.1016/j.msea.2017.09.041.

[28] GAO Chao-feng, XIAO Zhi-yu, ZOU Hai-ping, LIU Zhong-qiang, CHEN Jin, LI Shang-kui, ZHANG Da-tong. Characterization of spherical AlSi10Mg powder produced by double-nozzle gas atomization using different parameters [J]. Transactions of Nonferrous Metals Society of China, 2019, 29(2): 374−384. https://doi.org/10.1016/S1003-6326(19)64947-2.

[29] CHEN G, ZHAO S Y, TAN P, WANG J, XIANG C S, TANG H P. A comparative study of Ti−6Al−4V powders for additive manufacturing by gas atomization, plasma rotating electrode process and plasma atomization [J]. Powder Technology, 2018, 333: 38−46. https://doi.org/10.1016/j.powtec.2018.04.013.

[30] AHSAN M N, PINKERTON A J, MOAT R J, SHACKLETON J. A comparative study of laser direct metal deposition characteristics using gas and plasma-atomized Ti−6Al−4V powders [J]. Materials Science and Engineering A, 2011, 528: 7648−7657. https://doi.org/10.1016/j.msea.2011.06.074.

[31] NG G K L, JARFORS A E W, BI G, ZHENG H Y. Porosity formation and gas bubble retention in laser metal deposition [J]. Applied Physics A, 2009, 97(3): 641−649. https://doi.org/10.1007/S00339-009-5266-3.

[32] GAO Yuan, ZHAO Ji-bin, ZHAO Yu-hui, WANG Zhi-guo, SONG Hong-wu, GAO Meng-qiu. Effect of processing parameters on solidification defects behavior of laser deposited AlSi10Mg alloy [J]. Vacuum, 2019, 167: 471−478. https://doi.org/10.1016/j.vacuum.2019.06.042.

[33] LV Fei, SHEN Li-da, Liang Hui-yin, Xie De-qiao, WANG Chang-jiang, TIAN Zong-jun. Mechanical properties of AlSi10Mg alloy fabricated by laser melting deposition and improvements via heat treatment [J]. Optik, 2019, 179: 8−18. https://doi.org/10.1016/j.ijleo.2018.10.112.

[34] FANG Peng-jun, XU Yi, LI Xing-gang, CHEN Ya. Influence of atomizing gas and cooling rate on solidification characterization of nickel-based superalloy powders [J]. Rare Metal Materials and Engineering, 2018, 47(2): 423−430. https://doi.org/10.1016/s1875-5372(18)30082-1.

[35] SANG Li-ming, XU Yi, FANG Peng-jun, ZHANG Hong-lin, CAI Yun-tao, LIU Xin-yu. The influence of cooling rate on the microstructure and phase fraction of gas atomized $NiAl_3$ alloy powders during rapid solidification [J]. Vacuum, 2018, 157: 354−360. https://doi.org/10.1016/j.vacuum.2018.08.057.

[36] NEIKOV O D. Atomization and granulation [M]//Handbook of non-ferrous metal powders. Oxford, Elsevier, 2019: 102−185. https://doi.org/10.1016/B978-1-85617-422-0.00005-7.

[37] TANG Jun-jie, NIE Yan, LEI Qian, LI Yun-ping. Characteristics and atomization behavior of Ti−6Al−4V powder produced by plasma rotating electrode process [J]. Advanced Powder Technology, 2019, 30(10): 2330−2337. https://doi.org/https://doi.org/10.1016/j.apt.2019.07.015.

[38] LI Xing-gang, FRITSCHING U. Spray Transport Fundamentals [M]. Cham: Springer International Publishing, 2017: 89−176. https://doi.org/ 10.1007/978-3-319-52689-8_4.

[39] HANN D B, CHERDANTSEV A V, AZZOPARDI B J. Study of bubbles entrapped into a gas-sheared liquid film [J]. International Journal of Multiphase Flow, 2018, 108: 181−201. https://doi.org/10.1016/j.ijmultiphaseflow.2018.07.001.

[40] LUO Sheng, WANG Hong-ze, GAO Zhen-yang, WU Yi, WANG Hao-wei. Interaction between high-velocity gas and liquid in gas atomization revealed by a new coupled simulation model [J]. Materials & Design, 2021, 212: 110264. https://doi.org/10.1016/j.matdes.2021.110264.

[41] JALAAL M, MEHRAVARAN K. Fragmentation of falling liquid droplets in bag breakup mode [J]. International Journal of Multiphase Flow, 2012, 47: 115−132. https://doi.org/10.1016/j.ijmultiphaseflow.2012.07.011.

[42] PILCH M, ERDMAN C A. Use of breakup time data and velocity history data to predict the maximum size of stable fragments for acceleration-induced breakup of a liquid drop [J]. International Journal of Multiphase Flow, 1987, 13: 741−757. https://doi.org/10.1016/0301-9322(87)90063-2.

[43] URIONABARRENETXEA E, MARTÍN J M, AVELLO A, RIVAS A. Simulation and validation of the gas flow in close-coupled gas atomisation process: Influence of the inlet

gas pressure and the throat width of the supersonic gas nozzle [J]. Powder Technology, 2022, 407: 117688. https://doi.org/10.1016/j.powtec.2022.117688.

[44] SHI Y T, LU W Y, SUN W H, ZHANG S D, YANG B J, WANG J Q. Pressure-dependent microstructure evolution of Fe-based amorphous alloy powders via high-pressure gas atomization [J]. Journal of Alloys and Compounds, 2022, 920: 166038. https://doi.org/10.1016/j.jallcom.2022.166038.

[45] MARKUS S, FRITSCHING U. Discrete break-up modeling of melt sprays [J]. International Journal of Powder Metallurgy, 2006, 42: 23−32.

[46] BOGNO A A, HENEIN H, UHLENWINKEL V, GÄRTNER E. Single fluid atomization fundamentals [M]. Cham: Springer International Publishing, 2017: 9−48. https://doi.org/10.1007/978-3-319-52689-8_2.

[47] VLACHOS N, CHANG I T H. Investigation of flow properties of metal powders from narrow particle size distribution to polydisperse mixtures through an improved Hall-flowmeter [J]. Powder Technology, 2011, 205: 71−80. https://doi.org/10.1016/j.powtec.2010.08.067.

[48] MELLMANN J, HOFFMANN T, FÜRLL C. Flow properties of crushed grains as a function of the particle shape [J]. Powder Technology, 2013, 249: 269−273. https://doi.org/10.1016/J.POWTEC.2013.06.035.

[49] THOMPSON S M, BIAN L, SHAMSAEI N, YADOLLAHI A. An overview of direct laser deposition for additive manufacturing; Part I: Transport phenomena, modeling and diagnostics [J]. Additive Manufacturing, 2015, 8: 36−62. https://doi.org/10.1016/j.addma.2015.07.001.

[50] MOEINFAR K H, KHODABAKHSHI F, KASHANI-BOZORG S F, MOHAMMADI M, GERLICH A P. A review on metallurgical aspects of laser additive manufacturing (LAM): Stainless steels, nickel superalloys, and titanium alloys [J]. Journal of Materials Research and Technology, 2022, 16: 1029−1068. https://doi.org/10.1016/j.jmrt.2021.12.039.

[51] HERZOG D, SEYDA V, WYCISK E, EMMELMANN C. Additive manufacturing of metals [J]. Acta Materialia, 2016, 117: 371−392. https://doi.org/https://doi.org/10.1016/j.actamat.2016.07.019.

[52] NGO T D, KASHANI A, IMBALZANO G, NGUYEN K T Q, HUI D. Additive manufacturing (3D printing): A review of materials, methods, applications and challenges [J]. Composites Part B: Engineering, 2018, 143: 172−196. https://doi.org/10.1016/J.COMPOSITESB.2018.02.012.

[53] WOLFF S J, WEBSTER S, PARAB N D, ARONSON B, GOULD B, GRECO A, SUN Tao. In-situ observations of directed energy deposition additive manufacturing using high-speed X-ray imaging [J]. JOM, 2020, 73: 189−200. https://doi.org/10.1007/s11837-020-04469-x.

[54] KIANI P, DUPUY A D, MA K K, SCHOENUNG J M. Directed energy deposition of AlSi10Mg: Single track nonscalability and bulk properties [J]. Materials & Design, 2020, 194: 108847. https://doi.org/10.1016/j.matdes.2020.108847.

[55] ZHAO Lv, SONG Lu-bin, SANTOS MACÍAS J G, ZHU Ya-xin, HUANG Min-sheng, SIMAR A, LI Zhen-huan. Review on the correlation between microstructure and mechanical performance for laser powder bed fusion AlSi10Mg [J]. Additive Manufacturing, 2022, 56: 102914. https://doi.org/10.1016/j.addma.2022.102914.

[56] HADADZADEH A, AMIRKHIZ B S, MOHAMMADI M. Contribution of Mg_2Si precipitates to the strength of direct metal laser sintered AlSi10Mg [J]. Materials Science and Engineering A, 2019, 739: 295−300. https://doi.org/10.1016/j.msea.2018.10.055.

雾化方法对铝合金粉末特征及激光定向能量沉积过程 3D 打印性能的影响

阮 刚[1]，梁钰栋[2]，李 干[1,3]，金 莹[4]，黎兴刚[1,2]

1. 南方科技大学 机械与能源工程系，深圳 518055；
2. 南方科技大学 材料科学与工程系，深圳 518055；
3. 香港城市大学 机械工程系，香港 999077；
4. 浙江亚通新材料股份有限公司，杭州 310030

摘 要：对比研究了工业规模生产的用于激光定向能量沉积工艺的气体雾化和旋转盘雾化铝合金粉末的性能。对粉末特性、打印工艺窗口以及打印件的质量、显微组织和力学性能进行了对比和讨论。结果表明，旋转盘雾化粉末在球形度、表面质量、内部缺陷、流动性和松装密度方面优于气体雾化粉末，并且在激光定向能量沉积部件制造过程中具有更大的打印工艺窗口；与气体雾化粉末相比，基于旋转盘雾化粉末成形的部件具有更高的尺寸精度、更少的内部缺陷、更均匀和更精细的显微组织以及更优异的力学性能。

关键词：金属增材制造；旋转盘雾化；气体雾化；AlSi10Mg 粉末；粉末原料

(Edited by Bing YANG)